
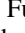




Induced anomalous Hall effect of massive Dirac fermions in ZrTe₅ and HfTe₅ thin flakesYanzhao Liu,¹ Huichao Wang ,² Huixia Fu ,³ Jun Ge,¹ Yanan Li,¹ Chuanying Xi ,⁴ Jinglei Zhang,⁴ Jiaqiang Yan,⁵ David Mandrus,^{5,6} Binghai Yan ,^{3,*} and Jian Wang ^{1,7,8,†}¹*International Center for Quantum Materials, School of Physics, Peking University, Beijing 100871, China*²*School of Physics, Sun Yat-Sen University, Guangzhou 510275, China*³*Department of Condensed Matter Physics, Weizmann Institute of Science, Rehovot 7610001, Israel*⁴*High Magnetic Field Laboratory, Chinese Academy of Sciences, Hefei 230031, Anhui, China*⁵*Materials Science and Technology Division, Oak Ridge National Laboratory, Oak Ridge, Tennessee 37831, USA*⁶*Department of Materials Science and Engineering, University of Tennessee, Knoxville, Tennessee 37996, USA*⁷*CAS Center for Excellence in Topological Quantum Computation, University of Chinese Academy of Sciences, Beijing 100190, China*⁸*Beijing Academy of Quantum Information Sciences, Beijing 100193, China*

(Received 6 September 2020; accepted 27 April 2021; published 14 May 2021)

Research on the anomalous Hall effect (AHE) has been lasting for a century to make clear the underlying physical mechanism. Generally, the AHE appears in magnetic materials, in which the extrinsic process related to scattering effects and intrinsic contribution connected with Berry curvature are crucial. Recently, AHE has been counterintuitively observed in nonmagnetic topological materials and attributed to the existence of Weyl points. However, the Weyl point scenario would lead to unsaturated AHE even in large magnetic fields and contradicts the saturation of AHE in several tesla (T) in experiments. In this work, we investigate the Hall effect of ZrTe₅ and HfTe₅ thin flakes in static ultrahigh magnetic fields up to 33 T. We find the AHE saturates to 55 (70) $\Omega^{-1} \text{cm}^{-1}$ for ZrTe₅ (HfTe₅) thin flakes above ~ 10 T. Combining detailed magnetotransport experiments and Berry curvature calculations, we clarify that the splitting of massive Dirac bands without Weyl points can be responsible for AHE in nonmagnetic topological materials ZrTe₅ and HfTe₅ thin flakes. This model can identify our thin flake samples to be weak topological insulators and serve as a tool to probe the band structure topology in topological materials.

DOI: [10.1103/PhysRevB.103.L201110](https://doi.org/10.1103/PhysRevB.103.L201110)

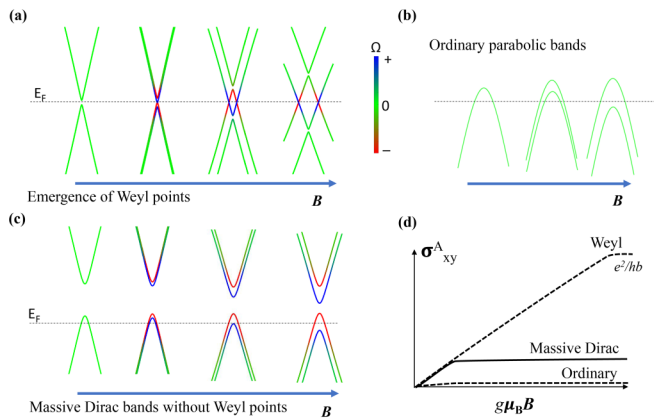
Anomalous Hall effect (AHE) is an important electrical transport phenomenon attracting extensive interest in both fundamental physics and potential applications [1,2]. Since the discovery of AHE in ferromagnetic iron in 1881 [3], the controversy of the microscopic mechanisms of AHE has lasted for almost a century. Two mechanisms have been identified nowadays: an extrinsic process related to scattering effects and an intrinsic contribution connected with Berry curvature [1,4–6]. The intrinsic AHE is quantitatively determined by the Berry curvature of the occupied states. Based on the theoretical developments, many experimental works of AHE in magnetic materials are convincingly explained by detailed band structure calculations [7–13]. Usually, time-reversal symmetry breaking by the magnetism is taken as the prerequisite for the AHE. Counterintuitively, nonmagnetic topological materials Cd₃As₂ and ZrTe₅ were recently found to show AHE or anomalous Nernst effect (ANE) [14–17] under the external magnetic field (B). In these materials, the Weyl points, which might be from the magnetic field induced Dirac points splitting, were believed to contribute to the AHE/ANE [18]. However, the Weyl point scenario leads to increasing AHE when the field continuously separates

Weyl points, until Weyl points annihilate and generate a three-dimensional (3D) quantized AHE, as shown in Figs. 1(a) and 1(d). This contradicts the fact that the AHE saturates in the field of several tesla (T) and presents a low plateau in previous experiments (the anomalous Hall conductivity (AHC) is usually tens of $\Omega^{-1} \text{cm}^{-1}$) [15,17].

Transition-metal pentatelluride ZrTe₅ and HfTe₅ have been studied since the 1970s due to their outstanding thermoelectric properties [19,20]. They are predicted [21] and confirmed to be topological materials with massive Dirac bands at the border between the strong and weak topological insulators (TIs). The electronic structures of ZrTe₅ and HfTe₅ are sensitive to the interlayer coupling and lattice parameters, which makes them promising platforms to study various intriguing phenomena including log-periodic quantum oscillations [22,23], 3D quantum Hall effect [24], negative magnetoresistance (NMR) [25,26], unconventional Hall effect [27,28], etc. However, the topological categorizations of these two materials are challenging because it is not easy for experiments to independently determine whether they are weak or strong TIs [29–34].

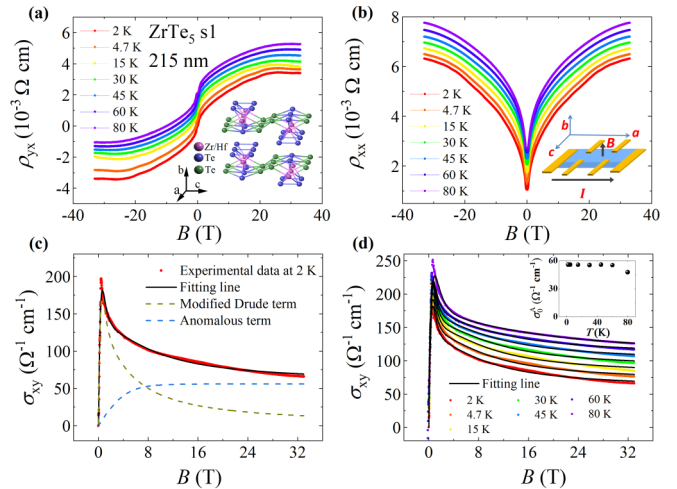
In ZrTe₅ and HfTe₅, clear nonlinear Hall traces are usually observed and the mechanisms for the Hall response are still under debate. The widely used two-carrier model tends to interpret the nonlinearity as the presence of more than one type of carriers [23–25,35,36]. On the other hand, Berry

*Corresponding author: binghai.yan@weizmann.ac.il†Corresponding author: jianwangphysics@pku.edu.cn



curvature induced AHE was claimed in the ZrTe₅ system, which also contributes to the nonlinearity of Hall traces [15,17]. The origin of the AHE in the nonmagnetic topological materials remains to be unambiguously and quantitatively clarified. The weak interaction between the layers of ZrTe₅ and HfTe₅ allows us to obtain flakes from the bulk by exfoliation [21]. The precisely aligned Hall bar structures obtained by micro- and nanofabrication processes are advantageous for measurements compared with previous works on bulk materials. More importantly, the high magnetic field is necessary to thoroughly investigate the field dependence of AHE.

In this work, we perform systematic magnetotransport measurements on ZrTe₅ and HfTe₅ flakes with thicknesses of about 210 nm in static ultrahigh magnetic fields up to 33 T. The nonlinear Hall resistance saturates at high magnetic fields, which cannot be explained by the classical Drude model. Because the magnetic field modifies the band structure by Zeeman splitting, it can sensitively change carrier densities of two spin channels. Thus, we develop an unusual Hall model with field-dependent carrier densities and explain the nonlinear Hall traces well. The AHE saturates to 55 (70) $\Omega^{-1} \text{cm}^{-1}$ for ZrTe₅ (HfTe₅) above a critical field ~ 10 T at 2 K. Our band structure calculations reveal that the nonzero Berry curvature from splitting massive Dirac bands leads to the saturated AHE, which does not necessarily require



the existence of Weyl points. We note that the Berry curvature intimately originates in the Dirac bands, whereas it cannot come from ordinary bands by Zeeman splitting, as illustrated in Figs. 1(b)–1(d). Furthermore, our model reveals that the strong and weak TIs exhibit opposite signs in the field-induced AHE and identifies our ZrTe₅ and HfTe₅ thin flakes to be weak TIs.

Figure 2 shows our magnetotransport results of a typical ZrTe₅ flake with a thickness of about 215 nm (*s1*). The Hall resistivity (ρ_{yx}) of *s1* at different temperatures is represented in Fig. 2(a). The ρ_{yx} grows sharply around 0 T, indicating a hole-dominated carrier type (p type). The slope of ρ_{yx} decreases with increasing B , finally leading to a saturated ρ_{yx} . Figure 2(b) shows the magnetic field dependence of longitudinal resistivity (ρ_{xx}). No obvious structures appear in ρ_{xx} up to 33 T, indicating that the saturation of ρ_{yx} is not due to the formation of an energy gap [24]. For clarity, data curves in Figs. 2(a) and 2(b) are shifted. Besides, we show the crystal structures of the layered materials with the space group $Cmcm$ in the inset of Fig. 2(a) [37]. The inset of Fig. 2(b) is the schematic of the Hall bar structure used for electrical transport measurements. The current is applied along the a axis and the field is always along the b axis.

We calculate the Hall conductivity (σ_{xy}) of *s1* at 2 K by the relation $\sigma_{xy} = \frac{\rho_{yx}}{\rho_{yx}^2 + \rho_{xx}^2}$ and plot σ_{xy} vs B in Fig. 2(c). Because ZrTe₅ is a nonmagnetic material and there is no

the existence of Weyl points. We note that the Berry curvature intimately originates in the Dirac bands, whereas it cannot come from ordinary bands by Zeeman splitting, as illustrated in Figs. 1(b)–1(d). Furthermore, our model reveals that the strong and weak TIs exhibit opposite signs in the field-induced AHE and identifies our ZrTe₅ and HfTe₅ thin flakes to be weak TIs.

Figure 2 shows our magnetotransport results of a typical ZrTe₅ flake with a thickness of about 215 nm (*s1*). The Hall resistivity (ρ_{yx}) of *s1* at different temperatures is represented in Fig. 2(a). The ρ_{yx} grows sharply around 0 T, indicating a hole-dominated carrier type (p type). The slope of ρ_{yx} decreases with increasing B , finally leading to a saturated ρ_{yx} . Figure 2(b) shows the magnetic field dependence of longitudinal resistivity (ρ_{xx}). No obvious structures appear in ρ_{xx} up to 33 T, indicating that the saturation of ρ_{yx} is not due to the formation of an energy gap [24]. For clarity, data curves in Figs. 2(a) and 2(b) are shifted. Besides, we show the crystal structures of the layered materials with the space group $Cmcm$ in the inset of Fig. 2(a) [37]. The inset of Fig. 2(b) is the schematic of the Hall bar structure used for electrical transport measurements. The current is applied along the a axis and the field is always along the b axis.

We calculate the Hall conductivity (σ_{xy}) of *s1* at 2 K by the relation $\sigma_{xy} = \frac{\rho_{yx}}{\rho_{yx}^2 + \rho_{xx}^2}$ and plot σ_{xy} vs B in Fig. 2(c). Because ZrTe₅ is a nonmagnetic material and there is no

contribution from the scattering of magnetic impurities to Hall response, we try to use the classical Drude model with one or two types of carriers to fit the σ_{xy} over the entire magnetic field range, as shown in Fig. S1(a) of the Supplemental Material [38–41]. However, both of the fitting lines cannot match the experimental data well. The discrepancy between the Drude model and experimental data was reported in SnTe/PbTe heterostructures and Bi₂O₂Se nanoplates, which show linear magnetoresistance [42,43]. However, the physics has not been fully understood. In our observation, the unusual saturation in the Hall resistivity recalls the AHE induced by Berry curvature [41]. As shown in Fig. S2(a) [38], the Hall conductivity can be only fitted by the classical Drude model in the weak magnetic field regime. The saturated discrepancy between the raw Hall conductivities and the Drude terms at large magnetic fields indicates the extra AHC contribution. We further adopt a different formula based on the theoretical scenario discussed in Fig. 1(c) and obtain satisfactory fitting results [black line in Fig. 2(c)] Details for the derivation of the empirical formulas are shown in the Supplemental Material [38]. The obtained empirical formulas are as follows:

$$\sigma_{xy}(B) = \sigma_{xy}^A(B) + \sigma_{xy}^N(B), \quad (1)$$

$$\sigma_{xy}^A(B) = \sigma_0^A \tanh(B/B_0), \quad (2)$$

$$\sigma_{xy}^N(B) = \left(\frac{n_0}{2} \left[1 + \tanh\left(\frac{B}{B_0}\right) \right] \mu_1^2 + \frac{n_0}{2} \left[1 - \tanh\left(\frac{B}{B_0}\right) \right] \mu_2^2 \right) eB. \quad (3)$$

Here, $\sigma_{xy}^A(B)$ [blue dashed line in Fig. 2(c), labeled as the anomalous term] is the B -dependent AHC and σ_0^A is the saturation value of σ_{xy}^A , B_0 is a parameter related to the saturation field, and σ_{xy}^A can reach $0.99\sigma_0^A$ at a critical field $B_c \sim 3B_0$, $\sigma_{xy}^N(B)$ [dark yellow dashed line in Fig. 2(c), labeled as the modified Drude term] is the contribution from both carriers with spin up or spin down under Lorentz force, n_0 is the total carrier density, and $\mu_{1,2}$ is the mobility of carriers with different spins. The fitting result indicates a total carrier density n_0 of about $2.8 \times 10^{17} \text{ cm}^{-3}$ and the mobilities of the two pockets are estimated to be $1.6 \times 10^4 \text{ cm}^2 \text{ V}^{-1} \text{ s}^{-1}$ and $3.7 \times 10^3 \text{ cm}^2 \text{ V}^{-1} \text{ s}^{-1}$. The relatively low carrier density of the sample indicates weak hole doping [44,45]. Figure 2(d) shows $\sigma_{xy}(B)$ at different temperatures. The temperature dependence of σ_0^A estimated from the fitting is shown in the inset of Fig. 2(d) and the critical field B_c as a function of temperature is plotted in the inset of Fig. S3 [38]. When the temperature is lower than 60 K, both σ_0^A and B_c are almost temperature independent with values of $55 \Omega^{-1} \text{ cm}^{-1}$ and 12 T, respectively. The slight drop of σ_0^A and enhancement of B_c at high temperatures may result from the smearing effect.

To further study the universality of AHE in transition-metal pentatelluride, we carried out electrical transport measurements on a HfTe₅ flake with a thickness of about 205 nm (s_2) at 2 and 5 K. Figure 3(a) shows the Hall resistivity of s_2 (p type) and the inset represents the ρ_{xx} vs B of s_2 . An obvious Hall plateau can be observed at large magnetic fields, similar to those results of the ZrTe₅ flake. The Hall conductivity of the HfTe₅ flake cannot be fitted by the classical Drude model

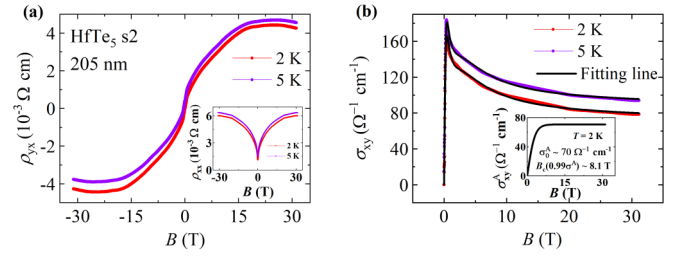


FIG. 3. Anomalous Hall effect in a HfTe₅ flake (s_2) with a thickness of about 205 nm. (a) Hall resistivity of s_2 versus B at 2 and 5 K. Inset: magnetic field dependence of longitudinal resistivity at 2 and 5 K. (b) Magnetic field dependence of Hall conductivity of s_2 . The black lines are fitting results based on our model. The inset shows the extracted anomalous Hall term of s_2 at 2 K. The saturation field (anomalous Hall conductivity) is estimated to be about 8.1 T ($70 \Omega^{-1} \text{ cm}^{-1}$). Purple curves in Figs. 3(a) and 3(b) are shifted for clarity.

either [Fig. S1(b)] [38]. Meanwhile, we notice that Eq. (3) could also well reproduce the AHC results as represented in Fig. 3(b). Purple curves in Figs. 3(a) and 3(b) are shifted for clarity. The inset of Fig. 3(b) shows the anomalous Hall contribution σ_{xy}^A of s_2 as a function of the magnetic field at 2 K. The total carrier density n_0 of s_2 is $1.8 \times 10^{17} \text{ cm}^{-3}$ at 2 K. Besides, the saturation field and value of σ_0^A are estimated to be about 8.1 T and $70 \Omega^{-1} \text{ cm}^{-1}$, respectively. The anomalous contribution in transport can also be supported by thermoelectric measurements. Figure S4 [38] represents the raw Nernst signals in a HfTe₅ flake with a thickness of about 210 nm (s_3). A clear steplike feature with a plateau can be observed in Nernst voltages at 5 and 10 K, consistent with the feature of ANE [14]. It is noted that the field scale of the saturation region is consistent between the raw data of Nernst voltage and Hall resistivity. The raw Nernst voltages are composed of the ordinary effect and the ANE contributed by the Berry curvature. Considering that the Mott relation is applicable to the intrinsic AHE and ANE [46], the field scale of the extracted ANE is expected to be close to that of the AHE [inset of Fig. 3(b)].

The weak temperature dependence of the σ_0^A , as shown above, indicates the intrinsic origin of the AHE in Dirac materials ZrTe₅ and HfTe₅. Most previous works attribute the AHE to the existence of Weyl points when the conduction and valence bands cross each other by the Zeeman splitting [15]. The Weyl point mechanism leads to unsaturated AHE even in large magnetic fields before the system reaches the 3D quantized AHE, which corresponds to $\sigma_0^A = \frac{e^2}{h} \frac{1}{b} \approx 260 \Omega^{-1} \text{ cm}^{-1}$ (b is the lattice parameter). However, the AHE saturates when the magnetic field is larger than ~ 10 T (the critical field B_c) in our work or ~ 2 T in the previous work [15]. The B_c difference may be due to the variation of the Fermi energy for different samples. Besides, the observed σ_0^A values are one order of magnitude smaller than $\frac{e^2}{h} \frac{1}{b}$. Therefore, we can rule out the Weyl point scenario in our experiment.

Different from ordinary bands, both massive and massless Dirac bands naturally exhibit Berry curvature if the double degeneracy is lifted. Heuristically, the Berry curvature of a specific band comes from the Dirac nature, and the

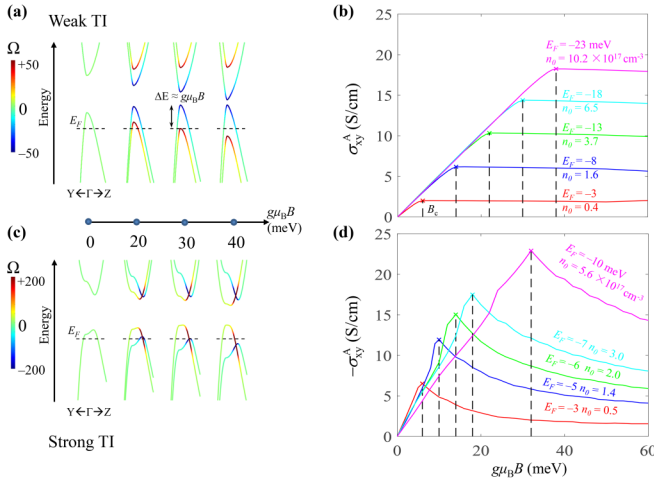


FIG. 4. The band structure and AHE evolution with respect to the Zeeman splitting. (a) The band dispersion near the Γ point for the weak TI phase. E_F is the Fermi level; ΔE denotes the energy splitting. (b) Anomalous Hall conductivity (σ_{xy}^A) with different carrier densities. σ_{xy}^A saturates after the critical field $g\mu_B B_c$. (c),(d) The band structure and σ_{xy}^A for the strong TI phase. AHE exhibits an opposite sign and no plateau, compared to the weak TI.

magnetic field can break the cancellation of Berry curvature from degenerate bands. In ZrTe_5 and HfTe_5 , the large Landé g factor [35,47,48] can generate sizable Zeeman splitting. As pointed out in previous calculations [21], the strong and weak TI phases depend sensitively on the lattice parameters. We build a Wannier function-based tight-binding Hamiltonian via *ab initio* density-functional theory (DFT) calculations on ZrTe_5 . Using the DFT-relaxed lattice parameters ($a = 4.03 \text{ \AA}$; $b = 15.00 \text{ \AA}$; $c = 13.79 \text{ \AA}$), we obtain a weak TI phase with massive Dirac bands near the Γ point and a small energy gap $E_g = 43 \text{ meV}$. Using the experimental lattice parameters ($a = 3.98 \text{ \AA}$; $b = 14.51 \text{ \AA}$; $c = 13.70 \text{ \AA}$) [36], we obtain a strong TI phase with massive Dirac bands near the Γ point with an indirect energy gap $E_g = 41 \text{ meV}$. Then we introduce a Zeeman energy $g\mu_B B/2$ to the system and investigate the band splitting $\Delta E \approx g\mu_B B$ for both weak and strong TI scenarios.

The energy bands are doubly degenerated without the Zeeman field. The Berry curvatures of two degenerate bands cancel each other exactly. Once an external magnetic field is applied along the b axis, the energy bands split into two with opposite Berry curvature. The Berry curvature distributes mainly in the band edge region, as a feature of the massive Dirac fermions. The nonzero Berry curvature on the Fermi surfaces induces the AHE since the Berry curvature from the Fermi sea is zero [6]. As bands split, the Fermi surface topology changes while the total carrier density remains the same. Therefore, we determine the new Fermi energy by fixing the total carrier density [n_0 in Eq. (3)] for each Zeeman energy. Then we integrate the Berry curvature over the corresponding Fermi surfaces [49] and obtain the AHC σ_{xy}^A . Based on our experiments, we set the carrier to be p type and focus on the top region of the valence bands, which are located near the Γ point. We check several carrier densities from 0.4 to $10.2 \times 10^{17} \text{ cm}^{-3}$ in calculations.

Figure 4(a) shows the evolution of the band structure of the weak TI phase. For increasing $g\mu_B B$, one Fermi surface expands in volume and the other shrinks until the smaller Fermi surface vanishes into a point and disappears at the critical field B_c . The critical field $g\mu_B B_c$ is proportional to the Fermi energy E_F , as shown in Fig. 4(b), where $E_F \approx g\mu_B B_c/2$ in the presence of strong spin-orbit coupling. After the critical field, the large Fermi surface remains unchanged because of the fixed total carrier density. For a very large field $g\mu_B B \approx 50 \text{ meV}$, the valence and conduction bands touch each other and induce Weyl points. Because their energy is still far from the Fermi level, the Weyl points weakly affect the Berry curvature on the Fermi surface. As shown in Fig. 4(b), the plateau feature remains nearly flat from 50 to 60 meV.

Based on our Fermi surface calculations, we find empirically $n_0 = 0.04 |E_F|^{1.77}$, where n_0 is in the unit of 10^{17} cm^{-3} and E_F is in the unit of meV. Therefore, we extract the g factor independently. From Fig. 2(c), we find the critical field $B_c = 12 \text{ T}$ and the total carrier density $n_0 = 2.8 \times 10^{17} \text{ cm}^{-3}$ and obtain $E_F = -11 \text{ meV}$ and $g \approx \frac{2|E_F|}{\mu_B B_c} = 32$ for ZrTe_5 flake $s1$. In Fig. 3(b), we have $B_c = 8.1 \text{ T}$ and $n_0 = 1.8 \times 10^{17} \text{ cm}^{-3}$ and obtain $E_F = -8.6 \text{ meV}$ and $g \approx \frac{2|E_F|}{\mu_B B_c} = 37$ for HfTe_5 flake $s2$. The obtained g factor is in agreement with previous measurement results [35,47,48]. It is noted that the theoretical σ_{xy}^A is in the same order of magnitude as the experiments. The smallness of the theoretical value may be due to the large Dirac mass ($E_g \sim 40 \text{ meV}$) used in the calculations, which sensitively depends on the sample condition [50]. Further experimental and theoretical investigations are needed to fully understand this discrepancy.

We also calculate the Fermi surfaces and the AHE for the strong TI phase, as shown in Figs. 4(c) and 4(d). For a weak TI, both the Γ and Z points have band inversions while the strong TI phase has a band inversion only at the Z point. For the weakly p -doped case, the Fermi surfaces are located around the Γ point. The mass of Dirac fermions at Γ is positive (negative) for the strong (weak) TI. Therefore, strong and weak TIs exhibit opposite signs of the Berry curvature for the same Zeeman splitting, which provides a qualitative criterion to distinguish the strong and weak phases. For the p -type carriers, the weak and strong TIs exhibit positive and negative, respectively, signs in the AHC. If the sample is n doped, the sign reverses compared to the p -doped case. Besides, a salient feature in the strong TI phase is the existence of Weyl points when two valence bands cross each other along the Γ - Z axis. The AHE is sensitively affected by Weyl points. Even after they are pushed below the Fermi energy after a critical field, the Weyl-point-induced Berry curvature remains on the Fermi surface. Instead of a plateau, the AHE decreases after this point. Because of both the positive value of σ_{xy}^A and the appearance of the plateau, we identify our thin flake samples to be weak topological insulators, which is consistent with previous spectroscopic reports [30,31,34].

In summary, the AHE in nonmagnetic materials ZrTe_5 and HfTe_5 was clearly demonstrated via transport measurements of thin flakes under perpendicular magnetic fields up to 33 T. We reveal that the massive Dirac nature leads to the AHE in the presence of the Zeeman splitting, without involving Weyl points. The model can further distinguish the strong and

weak TI phases by identifying the sign of the AHE, and our thin flake samples are characterized to be the weak TI. The results clearly clarify the AHE in transition-metal pentatellurides by high magnetic field measurements on flake samples with precise Hall bar and quantitative theoretical models. This work resolves important questions about the unusual AHE in nonmagnetic topological materials and provides a useful tool to distinguish strong/weak TIs by AHE analysis.

We thank X. Wu and W. Zhang for the help in related experiments. B.Y. acknowledges helpful discussions with Prof. J.-H. Chu. This work was financially supported by the National Key Research and Development Program of China (Grants No. 2018YFA0305604 and No. 2017YFA0303302), the National Natural Science Foundation of China (Grants No. 11888101, No. 11774008, and No. 12004441), Beijing Natural Science Foundation (Grant No. Z180010), and the Strategic Priority Research Program of Chinese Academy of

Sciences (Grant No. XDB28000000). J.Y. and D.M. were supported by the US Department of Energy, Office of Science, Basic Energy Sciences, Materials Sciences and Engineering Division. H.W. acknowledges the support of the Hundreds of Talents program of Sun Yat-Sen University and the Fundamental Research Funds for the Central Universities (Grant No. 201gpy165). B.Y. acknowledges the financial support by the Willner Family Leadership Institute for the Weizmann Institute of Science, the Benozio Endowment Fund for the Advancement of Science, Ruth and Herman Albert Scholars Program for New Scientists, the European Research Council (ERC) under the European Union's Horizon 2020 research and innovation program (ERC Consolidator Grant No. 815869, "NonlinearTopo"). C.X. was supported by the Users with Excellence Project of Hefei Science Center CAS (Grant No. 2018HSC-UE015).

Y.L., H.W., and H.F. contributed equally to this work.

-
- [1] N. Nagaosa, J. Sinova, S. Onoda, A. H. MacDonald, and N. P. Ong, *Rev. Mod. Phys.* **82**, 1539 (2010).
- [2] C. L. Chien and C. R. Westgate, *The Hall Effect and Its Applications* (Plenum, New York, 1980).
- [3] E. H. Hall, *Philos. Mag.* **12**, 157 (1881).
- [4] Z. Fang, N. Nagaosa, K. S. Takahashi, A. Asamitsu, R. Mathieu, T. Ogasawara, H. Yamada, M. Kawasaki, Y. Tokura, and K. Terakura, *Science* **302**, 92 (2003).
- [5] Y. Taguchi, Y. Oohara, H. Yoshizawa, N. Nagaosa, and Y. Tokura, *Science* **291**, 2573 (2001).
- [6] F. D. M. Haldane, *Phys. Rev. Lett.* **93**, 206602 (2004).
- [7] Y. G. Yao, L. Kleinman, A. H. MacDonald, J. Sinova, T. Jungwirth, D. S. Wang, E. G. Wang, and Q. Niu, *Phys. Rev. Lett.* **92**, 037204 (2004).
- [8] S. Nakatsuji, N. Kiyohara, and T. Higo, *Nature (London)* **527**, 212 (2015).
- [9] T. Suzuki, R. Chisnell, A. Devarakonda, Y.-T. Liu, W. Feng, D. Xiao, J. W. Lynn, and J. G. Checkelsky, *Nat. Phys.* **12**, 1119 (2016).
- [10] K. S. Takahashi, H. Ishizuka, T. Murata, Q. Y. Wang, Y. Tokura, N. Nagaosa, and M. Kawasaki, *Sci. Adv.* **4**, eaar7880 (2018).
- [11] E. Liu, Y. Sun, N. Kumar, L. Muechler, A. Sun, L. Jiao, S.-Y. Yang, D. Liu, A. Liang, Q. Xu, J. Kroder, V. Süß, H. Borrmann, C. Shekhar, Z. Wang, C. Xi, W. Wang, W. Schnelle, S. Wirth, Y. Chen, S. T. B. Goennenwein, and C. Felser, *Nat. Phys.* **14**, 1125 (2018).
- [12] Q. Wang, Y. Xu, R. Lou, Z. Liu, M. Li, Y. Huang, D. Shen, H. Weng, S. Wang, and H. Lei, *Nat. Commun.* **9**, 3681 (2018).
- [13] K. Kim, J. Seo, E. Lee, K. T. Ko, B. S. Kim, B. G. Jang, J. M. Ok, J. Lee, Y. J. Jo, W. Kang, J. H. Shim, C. Kim, H. W. Yeom, B. I. Min, B.-J. Yang, and J. S. Kim, *Nat. Mater.* **17**, 794 (2018).
- [14] T. Liang, J. Lin, Q. Gibson, T. Gao, M. Hirschberger, M. Liu, R. J. Cava, and N. P. Ong, *Phys. Rev. Lett.* **118**, 136601 (2017).
- [15] T. Liang, J. Lin, Q. Gibson, S. Kushwaha, M. Liu, W. Wang, H. Xiong, J. A. Sobota, M. Hashimoto, P. S. Kirchmann, Z.-X. Shen, R. J. Cava, and N. P. Ong, *Nat. Phys.* **14**, 451 (2018).
- [16] J. L. Zhang, C. M. Wang, C. Y. Guo, X. D. Zhu, Y. Zhang, J. Y. Yang, Y. Q. Wang, Z. Qu, L. Pi, H. Z. Lu, and M. L. Tian, *Phys. Rev. Lett.* **123**, 196602 (2019).
- [17] Z. Sun, Z. Cao, J. Cui, C. Zhu, D. Ma, H. Wang, W. Zhuo, Z. Cheng, Z. Wang, X. Wan, and X. Chen, *npj Quantum Mater.* **5**, 36 (2020).
- [18] A. A. Burkov, *Phys. Rev. Lett.* **113**, 187202 (2014).
- [19] S. Furuseth, L. Brattas, and A. Kjekshus, *Acta Chem. Scand.* **27**, 2367 (1973).
- [20] T. Jones, W. Fuller, T. Wieting, and F. Levy, *Solid State Commun.* **42**, 793 (1982).
- [21] H. M. Weng, X. Dai, and Z. Fang, *Phys. Rev. X* **4**, 011002 (2014).
- [22] H. C. Wang, H. W. Liu, Y. A. Li, Y. J. Liu, J. F. Wang, J. Liu, J. Y. Dai, Y. Wang, L. Li, J. Q. Yan, D. Mandrus, X. C. Xie, and J. Wang, *Sci. Adv.* **4**, eaau5096 (2018).
- [23] H. Wang, Y. Liu, Y. Liu, C. Xi, J. Wang, J. Liu, Y. Wang, L. Li, S. P. Lau, M. Tian, J. Yan, D. Mandrus, J. Y. Dai, H. Liu, X. C. Xie, and J. Wang, *Natl. Sci. Rev.* **6**, 914 (2019).
- [24] F. Tang, Y. Ren, P. Wang, R. Zhong, J. Schneeloch, S. A. Yang, K. Yang, P. A. Lee, G. Gu, Z. Qiao, and L. Zhang, *Nature (London)* **569**, 537 (2019).
- [25] H. Wang, C.-K. Li, H. Liu, J. Yan, J. Wang, J. Liu, Z. Lin, Y. Li, Y. Wang, L. Li, D. Mandrus, X. C. Xie, J. Feng, and J. Wang, *Phys. Rev. B* **93**, 165127 (2016).
- [26] Q. Li, D. E. Kharzeev, C. Zhang, Y. Huang, I. Pletikosic, A. Fedorov, R. Zhong, J. Schneeloch, G. Gu, and T. Valla, *Nat. Phys.* **12**, 550 (2016).
- [27] J. Ge, D. Ma, Y. Liu, H. Wang, Y. Li, J. Luo, T. Luo, Y. Xing, J. Yan, D. Mandrus, H. Liu, X. C. Xie, and J. Wang, *Natl. Sci. Rev.* **7**, 1879 (2020).
- [28] P. Li, C. H. Zhang, J. W. Zhang, Y. Wen, and X. X. Zhang, *Phys. Rev. B* **98**, 121108(R) (2018).
- [29] G. Manzoni, L. Gragnaniello, G. Autes, T. Kuhn, A. Sterzi, F. Cilento, M. Zacchigna, V. Enenkel, I. Vobornik, L. Barba, F. Bisti, P. Bugnon, A. Magrez, V. N. Strocov, H. Berger, O. V. Yazyev, M. Foinin, F. Parmigiani, and A. Crepaldi, *Phys. Rev. Lett.* **117**, 237601 (2016).
- [30] X.-B. Li, W.-K. Huang, Y.-Y. Lv, K.-W. Zhang, C.-L. Yang, B.-B. Zhang, Y. B. Chen, S.-H. Yao, J. Zhou, M.-H. Lu, L. Sheng, S.-C. Li, J.-F. Jia, Q.-K. Xue, Y.-F. Chen, and D.-Y. Xing, *Phys. Rev. Lett.* **116**, 176803 (2016).

- [31] R. Wu, J.-Z. Ma, S.-M. Nie, L.-X. Zhao, X. Huang, J.-X. Yin, B.-B. Fu, P. Richard, G.-F. Chen, Z. Fang, X. Dai, H.-M. Weng, T. Qian, H. Ding, and S. H. Pan, *Phys. Rev. X* **6**, 021017 (2016).
- [32] H. Xiong, J. A. Sobota, S. L. Yang, H. Soifer, A. Gauthier, M. H. Lu, Y. Y. Lv, S. H. Yao, D. Lu, M. Hashimoto, P. S. Kirchmann, Y. F. Chen, and Z. X. Shen, *Phys. Rev. B* **95**, 195119 (2017).
- [33] J. Mutch, W.-C. Chen, P. Went, T. Qian, I. Z. Wilson, A. Andreev, C.-C. Chen, and J.-H. Chu, *Sci. Adv.* **5**, eaav9771 (2019).
- [34] P. Zhang, R. Noguchi, K. Kuroda, C. Lin, K. Kawaguchi, K. Yaji, A. Harasawa, M. Lippmaa, S. Nie, H. Weng, V. Kandyba, A. Giampietri, A. Barinov, Q. Li, G. D. Gu, S. Shin, and T. Kondo, *Nat. Commun.* **12**, 406 (2021).
- [35] Y. Liu, X. Yuan, C. Zhang, Z. Jin, A. Narayan, C. Luo, Z. Chen, L. Yang, J. Zou, X. Wu, S. Sanvito, Z. Xia, L. Li, Z. Wang, and F. Xiu, *Nat. Commun.* **7**, 12516 (2016).
- [36] P. Shahi, D. J. Singh, J. P. Sun, L. X. Zhao, G. F. Chen, Y. Y. Lv, J. Li, J. Q. Yan, D. G. Mandrus, and J. G. Cheng, *Phys. Rev. X* **8**, 021055 (2018).
- [37] S. Okada, T. Sambongi, and M. Ido, *J. Phys. Soc. Jpn.* **49**, 839 (1980).
- [38] See Supplemental Material at <http://link.aps.org/supplemental/10.1103/PhysRevB.103.L201110>, which includes Refs. [14,16,22,23,25,36,39–41], for more details of experimental methods, additional measurement data, and calculation parameters.
- [39] G. Kresse and J. Furthmüller, *Phys. Rev. B* **54**, 11169 (1996).
- [40] I. Souza, N. Marzari, and D. Vanderbilt, *Phys. Rev. B* **65**, 035109 (2001).
- [41] T. Liang, S. Kushwaha, J. Kim, Q. Gibson, J. Lin, N. Kioussis, R. J. Cava, and N. P. Ong, *Sci. Adv.* **3**, e1602510 (2017).
- [42] C.-W. Liu, F. Wei, K. Premasiri, S. Liu, S. Ma, Z. Zhang, and X. P. A. Gao, *Nano Lett.* **18**, 6538 (2018).
- [43] P. Li, A. Han, C. Zhang, X. He, J. Zhang, D. Zheng, L. Cheng, L.-J. Li, G.-X. Miao, and X.-X. Zhang, *ACS Nano* **14**, 11319 (2020).
- [44] T. Liang, Q. Gibson, M. N. Ali, M. Liu, R. J. Cava, and N. P. Ong, *Nat. Mater.* **14**, 280 (2015).
- [45] C.-L. Zhang, S.-Y. Xu, C. M. Wang, Z. Lin, Z. Z. Du, C. Guo, C.-C. Lee, H. Lu, Y. Feng, S.-M. Huang, G. Chang, C.-H. Hsu, H. Liu, H. Lin, L. Li, C. Zhang, J. Zhang, X.-C. Xie, T. Neupert, M. Z. Hasan, H.-Z. Lu, J. Wang, and S. Jia, *Nat. Phys.* **13**, 979 (2017).
- [46] Y. Pu, D. Chiba, F. Matsukura, H. Ohno, and J. Shi, *Phys. Rev. Lett.* **101**, 117208 (2008).
- [47] R. Y. Chen, Z. G. Chen, X. Y. Song, J. A. Schneeloch, G. D. Gu, F. Wang, and N. L. Wang, *Phys. Rev. Lett.* **115**, 176404 (2015).
- [48] G. L. Zheng, X. D. Zhu, Y. Q. Liu, J. W. Lu, W. Ning, H. W. Zhang, W. S. Gao, Y. Y. Han, J. Y. Yang, H. F. Du, K. Yang, Y. H. Zhang, and M. L. Tian, *Phys. Rev. B* **96**, 121401(R) (2017).
- [49] X. Wang, D. Vanderbilt, J. R. Yates, and I. Souza, *Phys. Rev. B* **76**, 195109 (2007).
- [50] Y. Jiang, Z. L. Dun, H. D. Zhou, Z. Lu, K.-W. Chen, S. Moon, T. Besara, T. M. Siegrist, R. E. Baumbach, D. Smirnov, and Z. Jiang, *Phys. Rev. B* **96**, 041101(R) (2017).